Visualizing Interfacial Energy Offset and Defects in Efficient 2D/3D Heterojunction Perovskite Solar Cells and Modules

Weichuang Yang, Bin Ding, Zedong Lin, Jingsong Sun, YuanYuan Meng, Yong Ding, Jiang Sheng,* Zhenhai Yang,* Jichun Ye,* Paul J. Dyson, and Mohammad Khaja Nazeeruddin*

Currently, the full potential of perovskite solar cells (PSCs) is limited by chargecarrier recombination owing to imperfect passivation methods. Here, the recombination loss mechanisms owing to the interfacial energy offset and defects are quantified. The results show that a favorable energy offset can reduce minority carriers and suppress interfacial recombination losses more effectively than chemical passivation. To obtain high-efficiency PSCs, 2D perovskites are promising candidates, which offer powerful field effects and require only modest chemical passivation at the interface. The enhanced passivation and charge-carrier extraction offered by the 2D/3D heterojunction PSCs has boosted their power conversion efficiency to 25.32% (certified 25.04%) for small-size devices and to 21.48% for a large-area module (with a designated area of 29.0 cm^2). Ion migration is also suppressed by the 2D/3D heterojunction, such that the unencapsulated small-size devices maintain 90% of their initial efficiency after 2000 h of continuous operation at the maximum power point.

1. Introduction

Organic–inorganic hybrid perovskite solar cells (PSCs) have achieved a new certified record power conversion efficiency (PCE) of 26.0%, approaching crystalline silicon solar cells (c-Si SCs) record efficiency of 26.8%.[1] In high-efficiency c-Si SCs, homojunctions and heterojunctions have been used to suppress recombination losses owing to chemical passivation (reducing interface defect densities) and field-effect passivation (lowering minority carrier concentrations and accelerating majority-carrier extraction).[2] Similarly, in PSCs, the PCE primarily depends on the charge-carrier extraction effectiveness of the heterojunction of the electron-/hole-transport layers (ETLs/HTLs) and the perovskite layer.[3] Consequently, numerous chemical and field-effect passivation materials have been evaluated to improve PCEs.[4] Homojunction perovskite obtained from solution-processed *n*-type perovskites and thermally evaporated *p*-type perovskites have been designed to overcome insufficient charge-carrier extraction.[5] Perovskites with different bandgaps have been used to construct heterojunctions, providing more effective passivation and charge extraction, even in the absence of an HTL.[6] Heterojunctions obtained from multidimensional

W. Yang, J. Sun, Y. Meng, J. Sheng, Z. Yang, J. Ye
Zhejiang Provincial Engineering Research Center of Energy
Optoelectronic Materials and Devices
Ningbo Institute of Materials Technology and Engineering
Chinese Academy of Sciences (CAS)
Ningbo 315201, P. R. China
E-mail: shengjiang@nimte.ac.cn; yangzhenhai@nimte.ac.cn; jichun.ye@nimte.ac.cn
W. Yang
University of Chinese Academy of Sciences
Beijing 100049, P. R. China

B. Ding, Y. Ding, P. J. Dyson, M. K. Nazeeruddin
Institut des Sciences et Ingénierie Chimiques
Ecole Polytechnique Fédérale de Lausanne (EPFL)
Lausanne CH-1015, Switzerland
E-mail: MdKhaja.Nazeeruddin@epfl.ch
Z. Lin
Guangdong Provincial Key Lab of Nano-Micro Materials Research
School of Chemical Biology and Biotechnology
Shenzhen Graduate School
Peking University
Shenzhen 518055, P. R. China
J. Sheng
Zhejiang Energy Group R&D 152
Xihu District, Hangzhou 310003, P. R. China
Z. Yang
School of Optoelectronic Science and Engineering & Collaborative Innovation Center of Suzhou Nano Science and Technology
Key Lab of Advanced Optical Manufacturing Technologies of Jiangsu Province & Key Lab of Modern Optical Technologies of Education Ministry of China
Soochow University
Suzhou 215031, P. R. China

**ADVANCED
SCIENCE NEWS**

www.advancedsciencenews.com
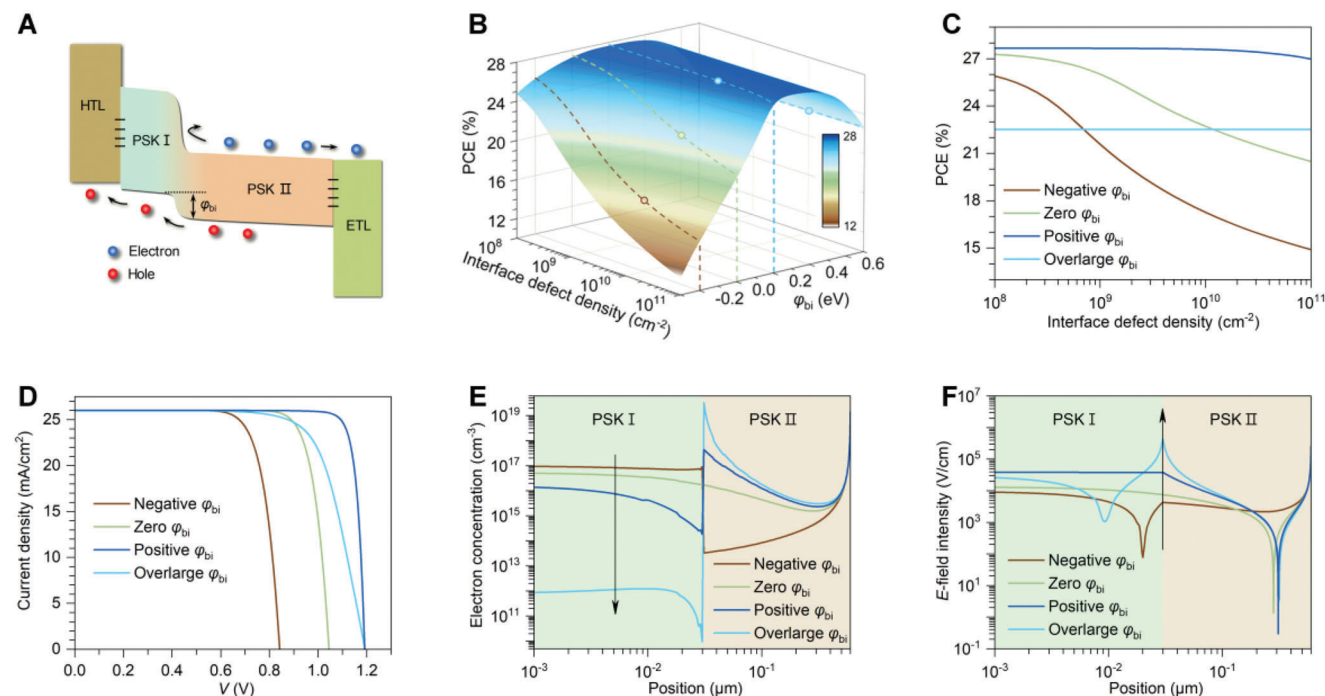
**ADVANCED
MATERIALS**

www.advmat.de

Figure 1. Illustration of the device physics for interfacial energy offset and defects in PSCs. A) An energy band diagram of PSCs with a heterojunction design. B) Simulated PCE as a function of φ_{bi} and the interfacial defect density at the perovskite and HTL interfaces, indicative of the influence of field-effect and chemical passivation mechanisms on the passivation quality, respectively. C) Cut-lines of PCE values versus the different interface defect densities under four representative φ_{bi} values, corresponding to the dotted lines in Figure 1B, i.e., −0.2, 0, 0.2, and 0.6 eV. D) Simulated $J–V$ curves for different φ_{bi} values, corresponding to the points in Figure 1B. E,F) Electron concentration distributions and cross-sectional E-field density versus the coordinate of perovskite from HTL to ETL.

perovskites are particularly attractive because of their high passivation quality and ease of fabrication.[4a] However, the intrinsic mechanisms and relationships between the passivation quality (chemical and field effects at the perovskite/ETL or HTL interfaces) and photovoltaic properties remain unclear.

In this study, we developed a device physics model to investigate chemical- and field-effect passivation mechanisms in regular PSCs with a perovskite–perovskite heterojunction. We identified that an appropriate energy offset (φ_{bi}) of 0.2 eV for the perovskite junctions increases the tolerance of interfacial defects by three orders of magnitude, reducing the preparation requirements. These findings provide direct guidance for the design of high-performance homo and heterojunction perovskite devices. To provide a feasible device scheme, an additional energy offset was constructed from a 2D perovskite layer at the interface between the perovskite and the HTL. Experiments and simulations demonstrated that this additional junction significantly improved charge-carrier transport/extraction and suppressed ion migration. By screening the halide types during 2D perovskite fabrication, we obtained an *n*-butylammonium iodide (BAI)-based PSC with a φ_{bi} of 0.15 eV, which achieved a small-size device PCE of 25.32% (certified 25.04%) and a module PCE of 21.39% (designated area of 29 cm²). The operational stability was also improved, maintaining 90% of the original PCEs after 2000 h of continuous output under 1 sun illumination.

2. Results and Discussion

2.1. Device Physics of Interfacial Energy Offset and Defects in PSCs

The influence of interfacial energy offset and defects on device performance was investigated by electrical simulations on a regular PSC structure, i.e., SnO_2/perovskite/spiro-OMeTAD (where perovskite = $Cs_{0.05}MA_{0.05}FA_{0.9}PbI_3$ and spiro-OMeTAD = 2,2′,7,7′-tetrakis[*N,N*-di(4-methoxyphenyl)amino]-9,9′-spirobifluorene], see **Figure 1**A. When the defect density at the HTL interface was reduced from 10^{11} to 10^8 cm⁻², the device PCE increased from 20.5% to 27.2%, implying that the efficiency potential is dependent on chemical passivation through suitable surface chemical grafting techniques (Figure 1B; Figure S1, Supporting Information). However, it is not possible to fill all of the interface charge defects using conventional dielectric materials. Hence, the influence of field-effect passivation on PCE was explored via appropriate band bending (i.e., a positive φ_{bi} of 0.2 eV) at the HTL/perovskite interface. The device obtained a high defect tolerance and maintained a high PCE (>27%) over a wide range of interface defect densities, from 10^8 to 10^{11} cm⁻² (Figure 1B,C). Figure 1D shows the current density–voltage ($J–V$) curves for various values of φ_{bi}. Both the open-circuit voltage (V_{OC}) and fill factor (FF) improved using a positive φ_{bi} value. To better understand this phenomenon, the electron concentration (minority carriers for hole transport) for different values of

φ_{bi} was determined, as shown in Figure 1E. The electron concentration lowers as the φ_{bi} value changes from negative to positive. Typically, a lower minority carrier concentration corresponds to a lower nonradiative recombination and a higher V_{OC}. Increasing φ_{bi} from −0.2 to 0.7 eV reduces the electron concentration by five orders of magnitude (from 10^{17} to 10^{12} cm^{-3}) at the HTL/perovskite interface, suggesting that the enhancement in V_{OC} at this interface is primarily determined by the suppression of recombination.

The concentration of charge-carriers is directly affected by the intensity of the electric field (*E*-field). Figure 1F shows the distributions of *E*-field intensities for different values of φ_{bi}. When the φ_{bi} value is negative (−0.2 eV), the perovskite near the HTL exhibits an *E*-field of < 10^4 V cm^{-1}. As φ_{bi} increases to 0.2 eV, the *E*-field is enhanced by one order of magnitude, reaching 10^5 V cm^{-1} (Figure 1F). It should be noted that although a stronger *E*-field can reduce the electron concentration as well as interface recombination, if φ_{bi} is too large (>0.4 eV) the carrier transport can be hindered by the interface potential barrier under maximum power point (MPP) conditions, resulting in a lower FF and PCE (Figure 1D).

These findings indicate that for an efficient PSC, the passivation quality must be improved by maximizing the suppression of nonradiative recombination at perovskite-related interfaces, which is dependent on both chemical and field-effect passivation. Chemical passivation requires saturating undercoordinated perovskite surface ions using appropriate compounds, whereas field-effect passivation can be achieved by a suitable energy offset that reduces the concentration of minority carriers at the related interfaces. Thus, high-quality passivation requires the full cooperation of chemical passivation to reduce surface defect densities and energy offsets to lower the concentration of minority carriers. In this study, the relationship between interfacial energy offset and defects was investigated using quantitative association rules, confirming that field-effect passivation caused by the energy offset plays a more significant role in PCE enhancement, providing a route to balance interface defect density and band bending for high-efficiency PSCs.

2.2. Fabrication and Characterization of the 2D/3D Perovskite Heterojunction

To improve the photovoltaic performance of PSCs by controlling the energy offset and defect density, a heterojunction of 2D/3D perovskites was introduced. The interlaminar molecules in 2D perovskites can effectively saturate the 3D perovskite surface to reduce surface defects during the fabrication process, leading to the formation of a potential energy offset for field-effect passivation. **Figure 2**A shows a schematic of the PSC (experimental details are provided in the Experimental Section, see Supporting Information). Two typical types of precursors, namely, BABr and BAI, were used to fabricate uniform 2D perovskite layers with thicknesses of ≈30 nm (Figure S2 and Note S1, Supporting Information). X-ray techniques confirmed the presence of the 2D perovskite layer, and grazing-incidence wide-angle scattering (GI-WAXS) was used to determine its orientation (Figure 2B; Figure S3, Supporting Information). The scattering patterns showed that the crystal orientation of 2D perovskite, by both BABr and

BAI post-treatments, was vertical and different from the polycrystal 3D perovskite, which has a random orientation (typical rings located at 0.97 Å^{-1}). The cut-lines along the q_z axis revealed three additional scattering vectors located at 0.30, 0.43, and 0.62 Å^{-1}, which were indexed to (020) (*n* = 2), (020) (*n* = 1), and (040) (*n* = 2), respectively (Figure 2C; Figure S3, Supporting Information). Similar results were obtained from the XRD patterns (Figure S4, Supporting Information). Moreover, no 2D-related signals were observed along the q_{xy} axis, indicating that the 2D perovskite orientation was mainly parallel to the substrate (Figure S3, Supporting Information). In addition, X-ray photoelectron spectroscopy (XPS) measurements demonstrated the effective interaction of the BA cation, indicating chemical grafting of the 2D perovskite (Figure S5 and Note S2, Supporting Information).[7]

Appropriate band alignment in 2D/3D perovskite heterojunctions is crucial for charge-carrier transport and is partially dependent on the alkyl molecules and *n* values of the 2D perovskite.[9] In this study, our aim was to tune the band alignment by selecting different halide types. To achieve this, we employed Kelvin probe force microscopy (KPFM) and ultraviolet photoelectron spectroscopy (UPS) to investigate the electrical properties of 2D/3D perovskite heterojunctions. The samples had a structure comprising a 2D/3D perovskite/ETL/FTO substrate, where the 2D perovskite was prepared using BAI and BABr precursors. Contact potential difference (CPD) mappings determined from KPFM measurements showed that the values increase from −602 mV for the bare 3D perovskite to −528 and −455 mV for the BABr and BAI cases, respectively (Figure 2D). This increase in CPD implies the creation of a potential barrier at the interface of the 2D/3D perovskite, resulting in a reduced work function. This band bending can be formed using a 2D/3D heterojunction, facilitating hole transport at the perovskite/HTL interface. The energy band values were estimated from UPS measurements (Figure 2E; Figure S7, Supporting Information), and the valence-band maximum (VBM) of the BABr-based and BAI-based 2D/3D heterojunction samples were found to be −5.75 and −5.65 eV, respectively, shallower than the value of −5.80 eV obtained for the 3D perovskite (Figure S8, Supporting Information), in agreement with the KPFM results.

Defect densities and charge transfer kinetics were investigated to further evaluate the charge-carrier dynamics of the 2D/3D perovskite heterojunction. The carrier profiles obtained from the capacitance characteristics suggest a reduced defect density for the samples with 2D perovskite, namely, 5.58×10^{16}, 4.53×10^{16}, and 3.67×10^{16} cm^{-3} for the control, BABr and BAI samples, respectively (Figure S9, Supporting Information),[10] indicating effective chemical passivation by the 2D perovskite. Next, the dynamics of charge-carrier extraction of the 2D/3D perovskite heterojunctions were analyzed using the charge-carrier lifetimes obtained from transient photoluminescence (TrPL) measurements (Figure 2F). The control, BABr, and BAI samples showed short/long lifetimes (τ_1/τ_2) of 177 ns/1.1 µs, 108 ns/3.6 µs, and 46 ns/2.6 µs, respectively (Table S3, Supporting Information).[11] The reduced short lifetimes τ_1 for the BABr and BAI samples reveal an improved extraction efficiency of charge-carriers, whereas the enhanced long lifetimes (i.e., τ_2) indicate reduced nonradiative recombination losses.[11] These improvements may be attributed to the presence of 2D/3D perovskite heterojunctions, which not only results in
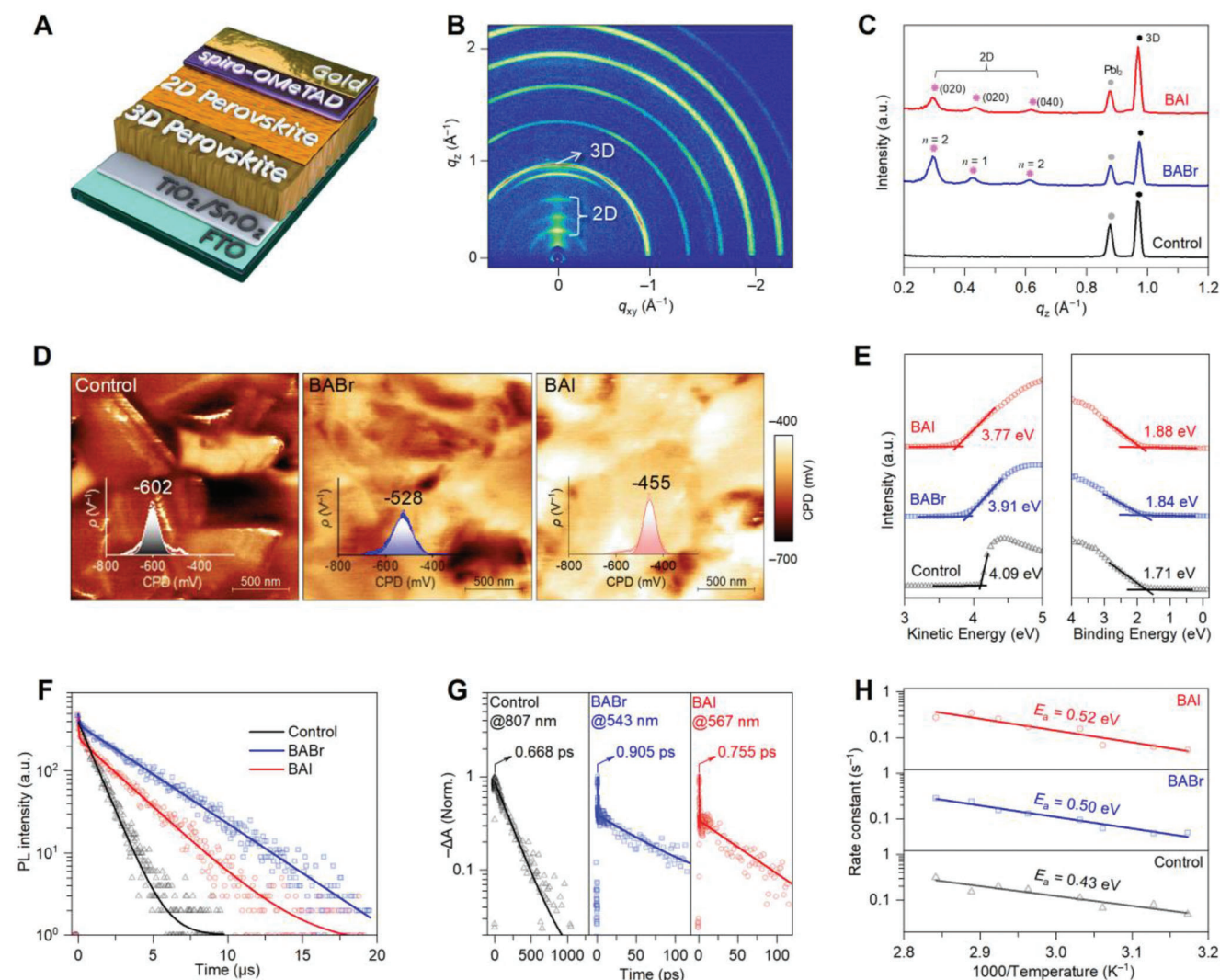
**ADVANCED
SCIENCE NEWS**
www.advancedsciencenews.com

**ADVANCED
MATERIALS**
www.advmat.de

Figure 2. Material structure and photoelectrical properties of the control perovskite and 2D/3D perovskite heterojunctions. A) Structure of the complete PSC, where the 2D perovskite is fabricated by post-treatment on the 3D perovskite surface. B) GIWAXS patterns of the 2D/3D perovskite with BAI post-treatment. C) Cut-lines of GIWAXS intensities along the q_z axis. Apart from the signs of PbI_2 and 3D perovskite, three additional scattering vectors are located at 0.31, 0.43, and 0.62 $Å^{-1}$ for both BABr and BAI, which are indexed to the (020) ($n = 2$), (020) ($n = 1$), and (040) ($n = 2$), respectively.[8] D) KPFM images and the corresponding statistical distributions. The corresponding surface morphology is shown in Figure S6 (Supporting Information). E–H) UPS spectra, TrPL decays, TAS decays, and Arrhenius plots by kinetic measurements.

chemical passivation, but also facilitates field-effect passivation and accelerates carrier extraction at the perovskite/HTL interface.

Further direct evidence of the charge-carrier extraction effect of the 2D/3D perovskite was obtained from ultrafast transient absorption spectroscopy (TAS), which confirmed the charge-carrier transfer from 3D to 2D perovskite. An 800 nm femtosecond laser was used as the light source, which has an energy higher than the bandgap of the 3D perovskite and lower than that of the 2D perovskite, to stimulate the free charge-carriers in the 3D perovskite. The TAS spectra only included ground-state bleaching (GSB) signals from the 3D perovskite, allowing us to study the transport processes of charge-carriers from the 3D to the 2D perovskite. The opened time of GSB signals of the 3D perovskite was determined to be 0.668 ps, and the signals of the samples with the 2D perovskite were delayed, with higher values of 0.905

and 0.755 ps for the BABr and BAI samples, respectively, confirming charge-carrier transport from the 3D to 2D perovskite (Figure 2G; Figures S10 and S11, Supporting Information).[12] The enhancement of carrier extraction and passivation for samples with 2D/3D heterojunctions was further demonstrated by steady-state PL measurements (Figure S12, Supporting Information), in good agreement with the TrPL and TAS data.

Additionally, the 2D/3D heterojunctions effectively suppress ion migration, which improves the long-term operating stability of the PSCs.[13] The activation energies for ion migration were evaluated using kinetic measurements.[14] By fitting the temperature-dependent photocurrent relaxation in the Arrhenius plot shown in Figure 2H, the apparent activation energy of ion migration was determined to be 0.43 eV for the control PSCs. In the 2D/3D PSCs, based on BABr and BAI systems, the acti-
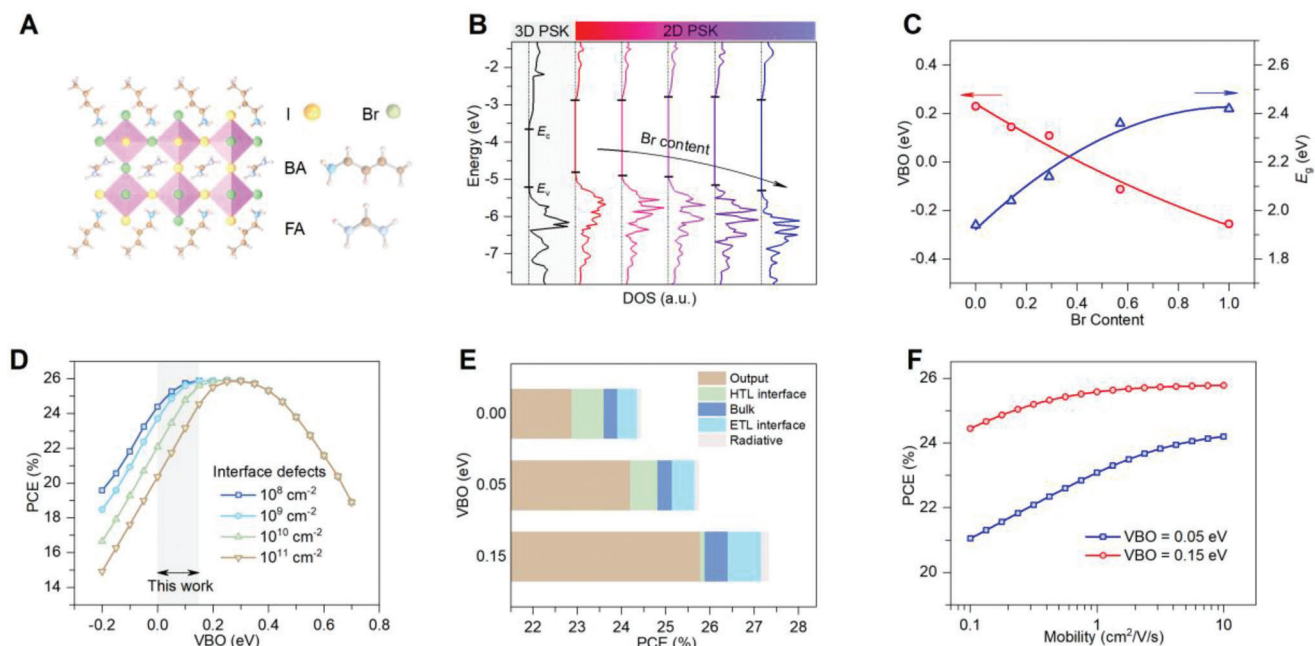
ADVANCED
SCIENCE NEWS

www.advancedsciencenews.com

ADVANCED
MATERIALS

www.advmat.de

Figure 3. Simulated energy structures and corresponding electrical performance of PSCs with 2D/3D heterojunction. A) Schematic model of 2D perovskite ($n = 2$) for DFT calculations. B) The DOS of 3D and 2D perovskite with the different Br^- content, namely, 0, 14%, 29%, 57%, and 100%. The E_v and E_c of the DOS are referenced to the vacuum energy level ($E_{vac} = 0$ eV) determined from the ionization potential and bandgap. C) Valence band offsets (VBOs) and bandgap (E_g) values versus Br^- content. D) PCE values versus the different VBO values under varying interface defect densities. The experimental range of this study is marked by the grey domain. E) Power output and free energy losses under MPP conditions. F) Simulated PCE values as a function of mobilities of the 2D perovskite in the case of VBO = 0.05 and 0.15 eV.

vation energy increases to 0.50 and 0.52 eV, respectively. This increase is usually attributed to the larger migration energy owing to the large distance between the interlayer spacings of the 2D perovskite.[15]

2.3. Numerical Screening of the 2D/3D Perovskite Heterojunctions in PSCs

Energy offset is crucial in achieving field-effect passivation.[16] To further understand the chemical and field-effect passivating effects of 2D/3D perovskite heterojunctions, the energy structures of 2D and 3D perovskites and their impact on device performance were investigated using density functional theory (DFT) calculations and finite-element simulations, respectively.[9a,17] The experimental results confirmed that the energy-band alignment was dependent on the halide type and content of the 2D perovskite. The effect of Br^- and I^- was investigated according to the schematic model shown in **Figure 3**A, where $n = 2$ was used to simplify the model. The total density of states (DOS) distributions reveal that perovskite with a higher Br^- content has a larger bandgap and a lower VBM, in accordance with experiment results (Figure 3B; Figures S14 and S15, Supporting Information).[18] The relative difference in the VBM between 2D and 3D perovskites, i.e., the valence band offsets (VBO, the φ_{bi} concerning hole extraction), was studied (Figure 3C). As the bromide content increases from 0 to 100%, the bandgap increases, but the VBOs gradually reduce from +0.23 to −0.26 eV. From the viewpoint of the energy band structure, the ability to tune the VBM and VBO

by altering the halide content is beneficial, as the optimal amount leads to the suppression of carrier recombination and promotes carrier extraction.

To investigate the impact of VBO on device performance, device physics was implemented into the model using previously reported parameters.[17d,e] The simulated $J–V$ curves showed good agreement with the experimentally determined curves (Figure S16, Supporting Information). The PCE of PSCs with various VBO values and interface defect densities of the perovskite/HTL layer were evaluated (Figure 3E; Figure S17, Supporting Information). The results showed that the PCE is highly dependent on VBO, particularly for cases with a high interface defect density. Excellent PCEs were achieved at a positive VBO (<0.42 eV) even with a high interface defect density (Figure S17, Supporting Information). As discussed previously, an energy difference at the heterojunction interface is required to achieve a high PCE, particularly if there is insufficient chemical passivation. The corresponding FF and V_{OC} tendencies also reveal that a mismatched VBO hinders charge-carrier transport at the interface of the perovskite/HTL layer and thus degrades the FF, whereas a reduced V_{OC} could only be obtained for cases with both a high interface defect density and a mismatched VBO (Figure S17, Supporting Information). Notably, the PCE values as a function of the VBO and interface defect densities revealed that from a range of experimental considerations (i.e., 0 < VBO < 0.15 eV), the PCE improved as the VBO increased or the interface defect density decreased (Figure 3D; the corresponding FF and V_{OC} plots are shown in Figure S18, Supporting Information). The distribution of the power output and recombination losses indicates
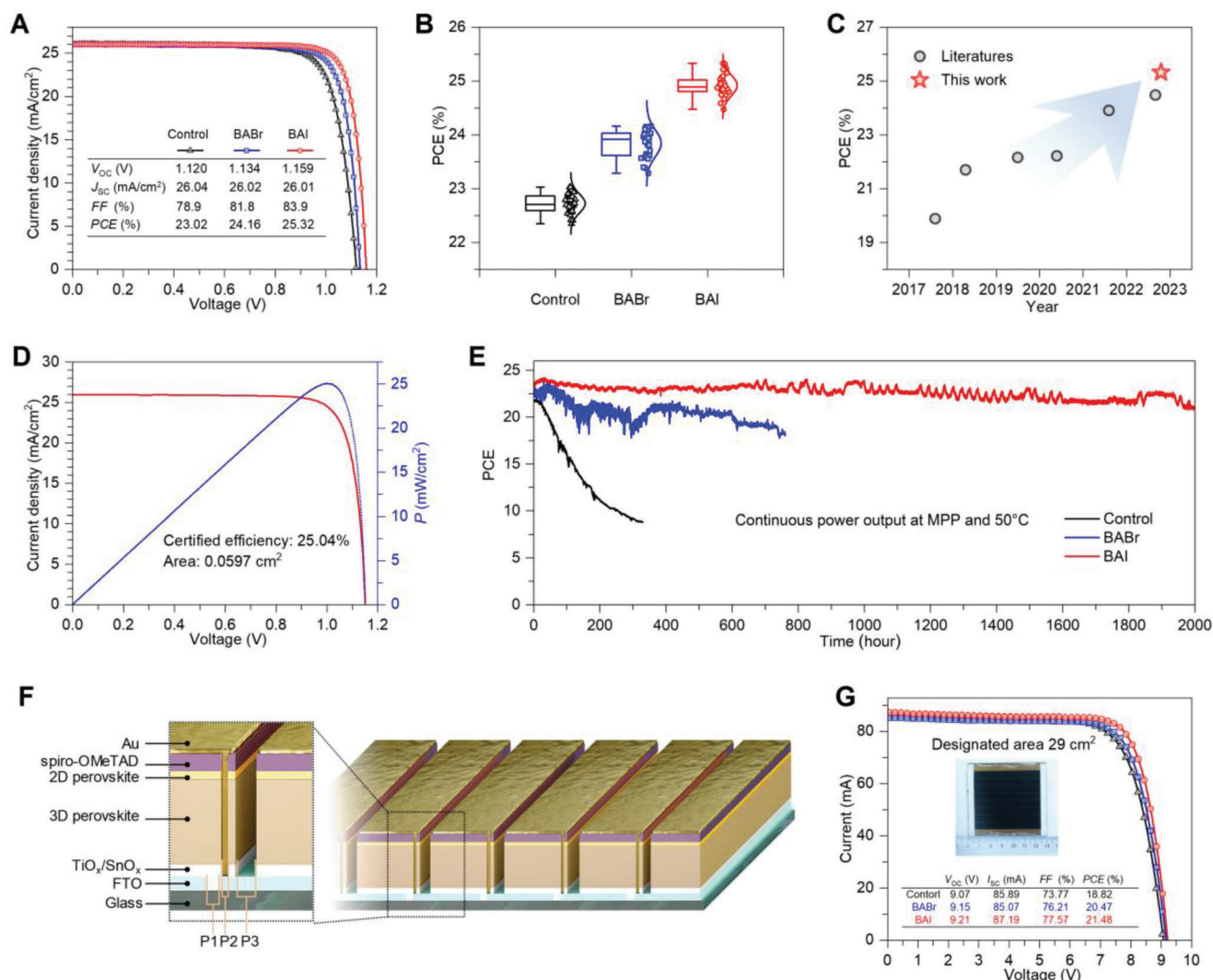
Figure 4. Performance of the 2D/3D PSC devices and modules. A) J–V curves of the champion cells. B) PCE statistics of 34 cells for each type. The box contains 50% of the data, the antenna shows the minimum and maximum values and the bars give the median. C) PCEs of 2D/3D perovskite-based PSCs reported in the literature and this work. The related values are collected in Table S4 (Supporting Information).[15,20] D) Certified J–V and P–V curves by Photovoltaic and Wind Power Systems Quality Test Center, IEE, Chinese Academy of Sciences for the BAI-based 2D/3D heterojunction PSCs. E) PCE of the PSCs under continuous illuminations at MPP operating conditions. F) A schematic of the PSC modules with nine sub-cells that are connected in series. G) J–V curve of the champion PSC modules tested with an aperture mask possessing a 29 cm^2 area; device image and electrical parameters are shown as well.

that the 2D/3D perovskite PSC could produce a higher power output and lower recombination loss at the HTL/perovskite interface compared to the 3D system (Figure 3E). Additionally, the electrical conductivity of 2D perovskites is lower than that of 3D perovskites in the vertical direction owing to the distance between the stratifications and the nonconductive alkyl chains.

To explore the influence of the electrical conduction of 2D perovskites on device performance completely, the PCE of the 2D/3D PSCs under various 2D perovskite mobilities were studied (Figure 3F). As the mobility of the 2D perovskite decreases from 10 to 0.1 cm^2 V^{-1} s^{-1}, there is a smaller reduction in PCE if the VBO is 0.15 eV than if it is 0.05 eV, suggesting that a proper VBO can compensate to some extent for a degradation in PCE due to low carrier mobility. Ion migration was also simulated (Figure

S19, Supporting Information), and it was shown to have a slight influence on PSC performance with adequate field-effect passivation. Therefore, the combination of chemical and field-effect passivation by 2D/3D perovskite can promote charge-carrier transport, have a high tolerance of the interface defects and carrier mobilities on the device performance, and thus relax the restriction of material selectivity of 2D perovskite and subsequent HTLs.

2.4. Photovoltaic Parameters and Stability of 2D/3D PSCs

Figure 4A and Figure S20 (Supporting Information) show the characteristic J–V curves of the champion devices for the three PSC types and their corresponding photovoltaic parameters.[19]

The control PSC exhibits a modest PCE of 23.02%, J_{SC} of 26.04 mA cm^{-2}, V_{OC} of 1.120 V, and FF of 78.9%. The BABr and BAI PSCs have a high PCE of 24.16%, and 25.32%, a favorable V_{OC} of 1.134 and 1.159 V and a remarkable FF of 81.8% and 83.9%, respectively. They exhibited steady-state PCE of 22.57%, 23.84%, and 25.04%, respectively (Figure S21, Supporting Information). The three devices showed similar J_{SC} values, and the external quantum efficiency (EQE) measurements for the three champion devices were in good agreement with the J–V results (Figure S22, Supporting Information). To assess device reproducibility, the photovoltaic parameters of 34 cells were collected and showed a tendency corresponding to that of the champion devices (Figure 4B; Figure S23, Supporting Information). The improved V_{OC}, FF, and PCE of the PSCs were further verified using transient photovoltage and electrochemical impedance spectroscopy, with the appearance of a longer photovoltage delay and reduced transport resistance for the 2D/3D perovskites (Figures S24 and S25, Supporting Information). The PCE value of 25.32% obtained is record-breaking for 2D/3D perovskite-based PSCs (Figure 4C). To confirm it, a BAI-based 2D/3D PSC was evaluated by an accredited laboratory. The test report showed a PCE of 25.04% with a high V_{OC} of 1.152 V, a remarkable J_{SC} of 25.986 mA cm^{-2}, and an excellent FF of 83.68% (Figure 4D; Figure S26, Supporting Information).

The stability of the devices during the long-term operation was assessed by recording their output power under continuous illumination (100 mW cm^{-2}) and at MPP conditions. The control PSC deteriorated rapidly, reaching 80% of the initial PCE in 100 h (T80). BABr-based PSC with 2D/3D heterojunctions exhibited improved stability with a T80 of 500 h. Notably, BAI-based PSCs with 2D/3D heterojunctions retained 90% of their initial values after 2000 h of operation (T90 = 2000 h). This finding is in good agreement with our device simulations and material characteristics, indicating that the 2D/3D perovskite heterojunction can suppress ion migration, affecting the long-term stability of PSCs.

The perovskites were also used to construct PSC modules to explore their performance in large-area devices (Figure 4F,G).[21] The modules were composed of nine sub-cells connected in series, with a designated area of 29 cm^2 (see the schematic diagram in Figure 4F and the photograph in Figure 4G). The average PCE of 16 PSC modules showed similar improvements in PCE (Figure S27, Supporting Information), with the champion BAI-based PSC module achieving a J_{SC} of 2.83 mA cm^{-2}, an FF of 80.3%, a V_{OC} of 9.416 V, and a PCE of 21.39% (Figure 4G).

3. Conclusion

For the first time, we quantified the relative contributions of the interfacial energy offset and defect density in 2D/3D perovskite heterojunctions and their effects on PSC. Furthermore, we showed how the value of φ_{bi} can be tuned to improve defect tolerance by three orders of magnitude and effectively suppress the non-radiative recombination losses. These fundamental studies enabled the development of 2D/3D perovskite heterojunctions with outstanding chemical and field-effect passivation, resulting in PSC modules with high PSC values. These findings provide a novel approach for designing highly efficient, stable, and large-scale PSCs.

Supporting Information

Supporting Information is available from the Wiley Online Library or from the author.

Conflict of Interest

The authors declare no conflict of interest.

Author Contributions

W.Y., B.D., and Z.L. contributed equally to this work. W.Y., J.S., and Y.D. conceived and designed the study. M.K.N. and J.Y. supervised it. W.Y., and B.D. designed, fabricated, and characterized the experimental samples and devices. Z.Y. conducted electrical simulations. Z.L. performed DFT calculations. Y.M. performed TAS measurements. J.S., W.Y., and Z.Y. interpreted the data and wrote the original draft, with contributions from the other authors. J.S., Y.D., J.Y., and M.K.N. reviewed and edited the final manuscript. All authors have revised the manuscript accordingly.

Data Availability Statement

The data that support the findings of this study are available in the supplementary material of this article.

[1] N. R. E. Laboratory, Best Research-Cell Efficiency Chart https://www.nrel.gov/pv/cell-efficiency.html, (accessed: May 2023).

[2] Z. Yang, Z. Liu, M. Cui, J. Sheng, L. Chen, L. Lu, W. Guo, X. Yang, Y. Zhao, W. Yang, J. C. Greer, Y. Zeng, B. Yan, J. Ye, *Cell Rep. Phys. Sci.* **2021**, *2*, 100667.

[3] a) J. Jeong, M. Kim, J. Seo, H. Lu, P. Ahlawat, A. Mishra, Y. Yang, M. A. Hope, F. T. Eickemeyer, M. Kim, Y. J. Yoon, I. W. Choi, B. P. Darwich, S. J. Choi, Y. Jo, J. H. Lee, B. Walker, S. M. Zakeeruddin, L. Emsley, U. Rothlisberger, A. Hagfeldt, D. S. Kim, M. Grätzel, J. Y. Kim, *Nature* **2021**, *592*, 381; b) H. Min, D. Y. Lee, J. Kim, G. Kim, K. S. Lee, J. Kim, M. J. Paik, Y. K. Kim, K. S. Kim, M. G. Kim, T. J. Shin, S. Il Seok, *Nature* **2021**, *598*, 444; c) Z. Dai, K. Yadavalli Srinivas, M. Chen, A. Abbaspourtamijani, Y. Qi, P. P. Nitin, *Science* **2021**, *372*, 618; d) Z. Li, B. Li, X. Wu, A. S. Stephanie, S. Zhang, D. Gao, J. L. Nicholas, Z. Zhu, *Science* **2022**, *376*, 416; e) M. Jeong, W. Choi In, M. Go Eun, Y. Cho, M. Kim, B. Lee, S. Jeong, Y. Jo, W. Choi Hye, J. Lee, J.-H. Bae, K. Kwak Sang, S. Kim Dong, C. Yang, *Science* **2020**, *369*, 1615.

[4] a) G. Wu, R. Liang, M. Ge, G. Sun, Y. Zhang, G. Xing, *Adv. Mater.* **2022**, *34*, 2105635; b) A. R. b. Mohd Yusoff, M. Vasilopoulou, D. G. Georgiadou, L. C. Palilis, A. Abate, M. K. Nazeeruddin, *Energy Environ. Sci.* **2021**, *14*, 2906; c) Z.-W. Gao, Y. Wang, W. C. H. Choy, *Adv. Energy Mater.* **2022**, *12*, 2104030.

[5] P. Cui, D. Wei, J. Ji, H. Huang, E. Jia, S. Dou, T. Wang, W. Wang, M. Li, *Nat. Energy* **2019**, *4*, 150.

[6] X. Yang, Q. Li, Y. Zheng, D. Luo, Y. Zhang, Y. Tu, L. Zhao, Y. Wang, F. Xu, Q. Gong, R. Zhu, *Joule* **2022**, *6*, 1277.

[7] S. Jeong, S. Seo, H. Yang, H. Park, S. Shin, H. Ahn, D. Lee, J. H. Park, N. G. Park, H. Shin, *Adv. Energy Mater.* **2021**, *11*, 2102236.

[8] G. Yang, Z. Ren, K. Liu, M. Qin, W. Deng, H. Zhang, H. Wang, J. Liang, F. Ye, Q. Liang, H. Yin, Y. Chen, Y. Zhuang, S. Li, B. Gao, J. Wang, T. Shi, X. Wang, X. Lu, H. Wu, J. Hou, D. Lei, S. K. So, Y. Yang, G. Fang, G. Li, *Nat. Photonics* **2021**, *15*, 681.

[9] a) G. Kresse, J. Furthmüller, *Comput. Mater. Sci.* **1996**, *6*, 15; b) T. Niu, Y.-M. Xie, Q. Xue, S. Xun, Q. Yao, F. Zhen, W. Yan, H. Li, J. L. Brédas, H. L. Yip, Y. Cao, *Adv. Energy Mater.* **2022**, *12*, 2102973; c) Y. W. Jang, S. Lee, K. M. Yeom, K. Jeong, K. Choi, M. Choi, J. H. Noh, *Nat. Energy* **2021**, *6*, 63.

[10] A. Matsushita, M. Yanagida, Y. Shirai, K. Miyano, *Sol. Energy Mater. Sol. Cells* **2021**, *220*,110854.

[11] L. Krückemeier, B. Krogmeier, Z. Liu, U. Rau, T. Kirchartz, *Adv. Energy Mater.* **2021**, *11*, 2003489.

[12] J. Liu, J. Leng, K. Wu, J. Zhang, S. Jin, *J. Am. Chem. Soc.* **2017**, *139*, 1432.

[13] G. Grancini, M. K. Nazeeruddin, *Nat. Rev. Mater.* **2019**, *4*, 4.

[14] C. Eames, J. M. Frost, P. R. F. Barnes, B. C. O'Regan, A. Walsh, M. S. Islam, *Nat. Commun.* **2015**, *6*, 7497.

[15] Q. Yao, Q. Xue, Z. Li, K. Zhang, T. Zhang, N. Li, S. Yang, C. J. Brabec, H.-L. Yip, Y. Cao, *Adv. Mater.* **2020**, *32*, 2000571.

[16] Z. Yang, H. Lin, K. W. A. Chee, P. Gao, J. Ye, *Nano Energy* **2019**, *61*, 221.

[17] a) A. Binek, F. C. Hanusch, P. Docampo, T. Bein, *J. Phys. Chem. Lett.* **2015**, *6*, 1249; b) J. P. Perdew, K. Burke, M. Ernzerhof, *Phys. Rev. Lett.* **1996**, *77*, 3865; c) V. Wang, N. Xu, J.-C. Liu, G. Tang, W.-T. Geng, *Comput. Phys. Commun.* **2021**, *267*, 108033; d) Z. Yang, W. Yang, X. Yang, J. C. Greer, J. Sheng, B. Yan, J. Ye, *Energy Environ. Sci.* **2020**, *13*, 1753; e) Y. Ding, B. Ding, H. Kanda, O. J. Usiobo, T. Gallet, Z. Yang, Y. Liu, H. Huang, J. Sheng, C. Liu, Y. Yang, V. I. E. Queloz, X. Zhang, J.-N. Audinot, A. Redinger, W. Dang, E. Mosconic, W. Luo, F. De Angelis, M. Wang, P. Dörflinger, M. Armer, V. Schmid, R. Wang, K. G. Brooks, J. Wu, V. Dyakonov, G. Yang, S. Dai, P. J. Dyson, et al, *Nat. Nanotechnol.* **2022**, *17*, 598; f) C. Freysoldt, B. Grabowski, T. Hickel, J. Neugebauer, G. Kresse, A. Janotti, C. G. Van de Walle, *Rev. Mod. Phys.* **2014**, *86*, 253; g) C. G. Van de Walle, J. Neugebauer, *J. Appl. Phys.* **2004**, *95*, 3851.

[18] T. J. Jacobsson, J.-P. Correa-Baena, M. Pazoki, M. Saliba, K. Schenk, M. Grätzel, A. Hagfeldt, *Energy Environ. Sci.* **2016**, *9*, 1706.

[19] B. Ding, S. Y. Huang, Q.-Q. Chu, Y. Li, C. X. Li, C. J. Li, G. J. Yang, *J. Mater. Chem. A* **2018**, *6*, 10233.

[20] a) Y. Bai, S. Xiao, C. Hu, T. Zhang, X. Meng, H. Lin, Y. Yang, S. Yang, *Adv. Energy Mater.* **2017**, *7*, 1701038; b) Y. Cho, A. M. Soufiani, J. S. Yun, J. Kim, D. S. Lee, J. Seidel, X. Deng, M. A. Green, S. Huang, A. W. Y. Ho-Baillie, *Adv. Energy Mater.* **2018**, *8*, 1703392; c) Y. Liu, S. Akin, L. Pan, R. Uchida, N. Arora, V. Milić Jovana, A. Hinderhofer, F. Schreiber, R. Uhl Alexander, M. Zakeeruddin Shaik, A. Hagfeldt, M. I. Dar, M. Grätzel, *Sci. Adv. 5*, eaaw2543; d) D. Zhao, D. Gao, X. Wu, B. Li, S. Zhang, Z. Li, Q. Wang, Z. Wu, C. Zhang, W. Choy, X. Zhong, Q. He, Z. Zhu, *Adv. Mater.* **2022**, *34*, 2204661;

[21] L. L. Gao, L. S. Liang, X. X. Song, B. Ding, G. J. Yang, B. Fan, C. X. Li, C. J. Li, *J. Mater. Chem. A* **2016**, *4*, 3704.

2302071 (8 of 8)